Perinatal correlated retinal activity is required

for the wiring of visual axons in non-image forming nuclei

Santiago Negueruela[1, 2#], Cruz Morenilla[1#], Macarena Herrera[1], Yaiza Coca[1], Danny Florez-Paz[1, 3], Maria Teresa López-Cascales[1], Ana Gomis[1] and Eloísa Herrera[1*]

[1]Instituto de Neurociencias de Alicante (Consejo Superior de Investigaciones Científicas-Universidad Miguel Hernández, CSIC-UMH). Campus San Juan, Ave. Ramón y Cajal s/n, 03550 San Juan de Alicante (Spain)

[2] Telethon Institute of Genetics and Medicine, Via Campi Flegrei 34, 80078 Pozzuoli NA, Italy.

[3] Columbia University, Department of Neurology, Motor Neuron Center. P&S Building Room 4-401, 630 W 168th St. New York, NY, 10032. USA.

# Equal contribution

* Author for correspondence: e.herrera@umh.es.

Phone: +34-965-919231 Fax: +34-965-919200

Keywords: Axon Remodeling, retinal spontaneous activity, Kir2.1, visual targets, suprachiasmatic nucleus

ABSTRACT

The formation of the visual system is a complex multistep process that includes proper assembly between retinal ganglion cell (RGC) axon terminals and their relay neurons in the different visual nuclei of the brain. RGC axons reach the main image-forming nuclei (IFN) —the superior colliculus and the lateral geniculate nucleus— at perinatal stages and extensively arborize to then refine throughout the first postnatal weeks. Spontaneous activity generated in the immature retina plays an essential role in the fine-tune refinement of exhuberant axonal arborizations but the molecular mechanisms underlying this activity-dependent remodeling process remain poorly characterized. RGC axons, in addition to innervate IFN, target non-image forming nuclei (NIFN), but the impact of spontaneous retinal activity in the development of these accessory nuclei has not yet been described. Here, by genetically altering spontaneous activity in the RGCs of mice we demonstrate that correlated retinal activity also shapes the connectivity of the non-image forming circuit and identify the transcriptional programs modulating this process. Together, our data contribute to a better understanding of the molecular mechanisms ruling activity-dependent axon refining in the building of visual circuits.

INTRODUCTION

Retinal ganglion cells (RGCs) are the neurons in the eye that collect visual information from other retinal neurons and send it to the brain. RGC axons project to different targets that may be classified as image-forming (IFN) and non-image forming nuclei (NIFN). IFN include the dorsal lateral geniculate nucleus of the thalamus (dLGN) and the superior colliculus (SC), both essential for sight processing. While the SC directs visually-guided behaviors, the dLGN relays visual information to the cortex for a deeper conscious visual perception (Stryker and Schiller, 1975). Neighboring RGCs projecting to neighboring cells in the dLGN and the SC form a continuous topographic map that reflects the image projected in the retina (Chalupa and Snider, 1998; Godement et al., 1984; Rakic, 1976). Thus, in the IFN the spatial relationship among the RGCs in the retina is maintained as an orderly representation (map) of the visual space. In addition to form topographic maps in the dLGN and SC, RGC axons project in an eye-specific manner in most mammals. In mice, axons from a subpopulation of RGC located in the ventrotemporal retina project to the SC and dLGN in the same hemisphere (ipsilateral RGCs), while the rest of RGC axons cross the brain midline and project to the opposite side (contralateral RGCs). Ipsi and contralateral terminals first overlap at early postnatal stages in the dLGN but eventually segregate to finally rearrange into complementary non-overlapping domains in the mature visual system (Godement et al., 1984).

Both the formation of a raw retinotopic map and the targeting of ipsi and contralateral visual terminals at the SC and the thalamus are initially governed by guidance and adhesion molecules (Nakamoto et al., 2019; Su et al., 2021). In rodents, spontaneous waves of correlated activity triggered by starbust amacrine cells and transmitted to RGCs, refine and prepare the network to receive environmental stimuli when eyes open around two weeks after birth (Demas et al., 2003; Galli and Maffei,

1988; McLaughlin et al., 2003; Pak et al., 2004; Torborg et al., 2005; Torborg and Feller, 2005; Wong et al., 1993).

In addition to project to IFN, RGC axons project to NIFN such as the olivary pretectal nucleus (OPN), the nucleus of the optic tract (NOT) or the suprachiasmatic nucleus (SCN). The OPN and NOT mediate the pupillary reflex (Young and Lund, 1994) and saccadic movements (Kato et al., 1986) for image stabilization while the SCN regulates entrainment of the circadian clock, hormone rhythms and sleep cycles (Dhande et al., 2013; Hattar et al., 2003; Noseda and Burstein, 2011; Yonehara et al., 2009). Correlated retinal activity encodes positional information essential for the remodeling of RGC axons at the IFN but the impact of spontaneous retinal activity on NIFN has not been investigated. NIFN receive inputs from the intrinsically photosensible retinal ganglion cells (ipRGCs), a particular type of RGCs that responds directly to light and expresses melanopsin photopigment (OPN4) (Berson et al., 2002; Do and Yau, 2010; Hattar et al., 2002; Schmidt and Kofuji, 2011). NIFN work unconsciously to indirectly support vision without apparent need to transmit spatial information. Therefore, the organization of RGC axons in topographic maps and eye-specific projection patterns may not be as evident or even absent in NIFN. On the other hand, the molecular mechanisms that shape the circuit by transducing retinal spontaneous activity in axon remodelling at the targets remain largely unknown.

To determine the impact of spontaneous retinal activity in NIFN and identify axon remodeling-mechanisms influenced by correlated neuronal activity, we generated several transgenic mouse lines with uncorrelated spontaneous activity and characterized the arborizations of RGC at different visual nuclei. Overall, our results demonstrate that perinatal correlated retinal activity is essential for the establishement of proper connectivity in both image-forming and non-image forming visual circuits. In addition, the transcriptomic analysis of postnatal retinas from mutant mice with altered patterns of retinal activity retrieved molecular programs that respond to correlated spontaneous activity and are responsible for the refinement of retinal axons.

RESULTS

Generation and characterization of mice ectopically expressing Kir2.1 in RGCs

To investigate the function of spontaneous correlated retinal activity in NIFN and the underlying activity-dependent genetic program that modifies axon remodeling at the visual targets, we aimed to generate a mouse line with disrupted embryonic retinal activity by conditionally expressing the rectifying potassium channel Kir2.1 in RGCs. We first generated a line containing hKir2.1 fused to the fluorescence protein eYFP in a cre-dependent manner (Kir2.1YFP^{flxStop}) and breed these mice with a Pou4f2-cre to drive gene expression in recently differentiated RGCs (Fuerst et al., 2012) obtaining double mutant mice Pou4f2-cre;Kir2.1YFP^{fxStop} (Pou4f2-Kir2.1 from now on) (**Fig. 1A**). The analysis of retinal sections from newborn Pou4f2-Kir2.1 mice confirmed strong expression of hKir2.1eYFP in the RGC layer compared to the retinas of control littermate mice (**Fig. 1B**).

To evaluate the impact of Kir2.1 ectopic expression in the excitability of RGCs, we performed whole cell recordings in the retinas of Pou4f2-Kir2.1 and control mice. Because YFP labelling was detectable only after antibody immunostaining, we crossed the Pou4f2-Kir2.1 line with a tdTomato reporter line (*Rosa26Stop-tdTm*) in order to visualize and record RGCs overexpressing Kir2.1 in semi-intact wholemount retinal preparations. As expected, the resting membrane potential of tdTomato RGCs recorded from postnatal Pou4f2-Kir2.1 mice (-50.7 ± 1.4 mV, n=21) was significantly lower than in neurons from control mice (-45.5 ± 1.9 mV, n=13) (**Fig. 1C**). In control mice, the large majority of RGCs responded with events (depolarization that not evoke an action potential) or bursts of activity separated by long refractory periods in the control retinas. A small number of cells showed train responses and few cells did not respond at all (**Fig. 1D, E**). In contrast, the amount of RGCs with train responses was doubled in the Pou4f2-Kir2.1 mice and unresponsive cells were not found in these mutants (**Fig. 1D, E)**. In addition, the frequency of bursts increased significantly in

Pou4f2-Kir2.1 (0.44 ± 0.10) compared to the control retinas (0.2 ± 0.08) **(Fig. 1F)**. Thus, similar to what it has been previously reported for thalamic neurons (Antón-Bolaños et al., 2019), these results showed that overexpression of Kir2.1 in retinal ganglion neurons changed the pattern of spontaneous activity, likely generating uncorrelated patterns of activity that presumably prevent the transmission of spatial information transmitted by retinal waves.

Next, we analyzed the projection pattern of ipsi and contralateral RGC terminals at the dLGN and the SC of these mice by injecting cholera toxin subunit B conjugated with far-red (CTB-Alx647) or green (CTB-Alx488) fluorophores into each eye (**Fig. 2A**) of P9 Pou4f2-Kir2.1 and control mice. Two days later, when axons are already refined but eyes still not open, anterograde axonal tracing was monitored in sections and iDISCO-clarified brains. As expected and in agreement with previous reports, we found that segregation between ipsilateral and contralateral terminals was almost finished in the dLGN of control mice and a well-defined ipsilateral territory with no presence of contralateral innervation was observed (Godement et al., 1984; Pham et al., 2001; Upton et al., 1999) (**Fig. 2B, 2D-D' and 2G**). However, in the Pou4f2-Kir2.1 mice contralateral terminals invade the ipsilateral region (**Fig. 2C, 2E-E' and 2G**), resulting in an increase of the unsegregated area (**Fig. 2F**) and a reduced area dominated only by ipsi innervation (**Fig. 2G**). Also, the area receiving ipsilateral innervation was expanded compared to the controls (**Fig. 2H**). The analysis of RGC axons at the SC also showed an aberrant refinement of ipsilateral RGC arborizations in Pou4f2-Kir2.1 mice compared to their control littermates (**Fig. S1**) but, because Pou4f2 is also expressed in the SC, we cannot rule out that axon refinement defects in this nucleus result from activity alterations in the collicular cells. Nevertheless, the lack of refinement in the thalamus confirms that correlated spontaneous retinal waves are essential for eye-specific refinement at the IFN and validate the Pou4f2-Kir2.1 mouse line as a model to investigate the impact of correlated spontaneous activity in the NIFN.

Spontaneous retinal activity in the NIFN

Correlated retinal activity is known to encode spatial information among neighboring RGCs. Since NIFN are not as functionally-related to spatial information and sight as IFN, we wondered to what extent, if at all, the alteration of spontaneous retinal waves affects the refinement of visual terminals in these nuclei. To address this, we analyzed axonal terminals at two NIFN, the olivary pretectal nucleus (OPN) and the suprachiasmatic nucleus (SCN).

The OPN is the largest of the seven nuclei that integrate the pretectal nuclei located in a region anterior to the SC. It is involved in mediating behavioral responses to acute changes in ambient light and the optokinetic reflex (Gamlin, 2006). We analyzed 3D images from this nucleus taken from clarified brains and serial coronal sections from Pou4f2-Kir2.1 and control mice previously injected with CTB-647 or CTB-488 into each eye (**Fig. 3A**). A larger number of ipsi and contralateral terminals overlapped in space in the OPN of Pou4f2-Kir2.1 mice compared to control littermates (**Fig. 3B-F**), indicating segregation defects in this nucleus as a consequence of disturbed retinal spontaneous activity.

Next, we analyzed the SCN of both Pou4f2-Kir2.1 and control littermantes. This nucleus, located in the diencephalon just behind the optic chiasm, is considered the circadian pacemaker and is responsible for controlling circadian rhythm. It is innervated only by intrinsically photosensitive RGCs that express melanopsin (OPN4) distributed all over the retina (Prigge et al., 2016; Sekaran et al., 2003). Melanopsin-RGCs can be activated by the retinal waves, and carry out modulatory effects even in the absence of light (Renna et al., 2011). Although the SCN is located closer to the retina compared to other visual nuclei, it is innervated at the same time than the SC and the dLGN with collateral branches invading this nucleus postnatally days after RGC axons decided to cross or not the midline at the optic chiasm region (Sekaran et al., 2005; Sernagor, 2005). Because most Pou4f2-RGCs do not project to the SCN (Chen et al., 2011), we used a second cre line (Slc6a4/Et33-Cre) that has been shown to drive gene

expression to a subset of RGCs that innervate the SCN (Su et al., 2021) to investigate the function of retinal spontaneous activity in this nuclei. The serotonin transporter (Slc6a4) is specifically expressed in a subpopulation of RGCs located at the ventrotemporal retina that project ipsilaterally to the IFN (García-Frigola and Herrera, 2010; Marcucci et al., 2016). The offspring of Slc6a4-cre mice breed with a TdTomato reporter mice (*Slc6a4/Et33-Cre; Rosa26-stop^{loxP}-tdTomato*) labels ipsilaterally projecting RGCs and we observed that about 4% of the Slc6a4/TdTm cells were also positive for OPN4 (**Fig. 4A, A'**), suggesting that they are iRGCs that also project to the SCN.

To investigate the influence of spontaneous waves in the wiring of visual input at the SCN, we first verified that activity was disturbed in the Slc6a4/TdTomato-cells by patch-clamp recordings as we previously did for the Pou4f2-Kir2.1/TdTomato mice. The resting membrane potential of TdTomato RGCs recorded from postnatal Slc6a4-Kir2.1 mice (-55.1 ± 1.5 mV) was significantly below that of tdTomato RGCs recorded from the control mice (-46.4 ± 2.6 mV) (**Fig. S3A**). As in the other Kir2.1 line, the number of bursts increased significantly in the Slc6a4-Kir2.1/TdTomato (0.63 ± 0.01) retinas compared to the controls (0.24 ± 0.11) whereas the number of events in Slc6a4-Kir2.1/TdTomato retinas significantly decreased (0.35 ± 0.09 vs 0.87 ± 0.13) **(Fig. S3C-D)**.

To investigate the impact of spontaneous activity in the retinal terminals projecting to the SCN, we injected CTB-488 and CTB-647 into the eyes of *Slc6a4/Et33-Cre; Rosa26-stop^{loxP}-tdTomato* (Slc6a4-TdTm) mice to distinguish RGC-derived terminals from the non-retinal innervations (**Fig. S3E**). Far from being segregated, about 90% of the Slc6a4-terminals (tdTm/CTB-488) were located only 5µm apart from CTB-647 axons coming from the opposite eye (**Fig. S3F-H**), in line with previous studies reporting not eye-specific segregation of melanopsin RGC terminals in the SCN (Fernandez et al., 2016).

The distribution of RGC terminals at the SCN (**Fig. 4B**) was different in the Slc6a4-mice compared to the controls. Although TdTm/CTB-488 arborizations covered a similar area in Kir2.1 and control mice (**Fig. 4C**), the fluorescence detected in the ventrolateral area of the nucleus was significantly reduced in the Slc6a4-Kir2.1 mice, indicating that axonal arborizations are less dense and more scattered in the mutants (**Fig. 4C-D**). These results strongly suggested that, despite eye-specific segregation and topographic mapping are not evident features of the SCN, spontaneous activity before eye-opening also shapes the final innervation of RGCs in this nucleus.

Transcriptional changes governing spontaneous-dependent refinement in the visual targets

Accumulating evidences indicate that correlated neural activity and the associated calcium influx into the cytoplasm activate a cascade of genes that integrate the machinery required for normal refinement and synapse formation (Bito et al., 1997; West et al., 2001). However, the molecular programs that act downstream of spontaneous activity to mediate RGC axon remodeling at the target nuclei have not been characterized. To identify molecular mechanisms underlying activity dependent-axonal remodeling, we took advantage of the Kir2.1 conditional mice and compared the transcriptional profile of RGCs from mice expressing Kir2.1 (Pou4f2-Kir2.1; R26^{Td}Tomato) and control (Pou4f2-cre; R26^{Td}Tomato) mice at P4, the time when most RGC axon arbors are remodeling at the visual nuclei and also at P8 when the majority of the terminals are already refined (**Fig. 5A**). TdTomato-RGCs from Pou4f2-Kir2.1; R26^{Td}Tomato and control mice were purified by fluorescence activated cell sorting (FACS) to isolate total RNA and perform high-throughput sequencing of the samples (RNA-Seq). Principal Component Analysis (PCA) confirmed differential grouping of samples from each genotype at both stages (**Fig. S4**).

Analysis of transcriptional profiles of P4 and P8 Pou4f2-Kir2.1; R26^{Td}Tomato mice and their respective controls revealed different transcriptional programs

deregulated at each stage (**Fig. 5B**) that likely reflects the switch from cholinergic to glutamatergic dependent axonal remodelling and from a non-assembled to an assembled circuit. We found 468 genes differentially expressed (DEG) at P4 and 1533 at P8 between mutant and control retinas; 232 were upregulated and 236 downregulated at P4 and 895 downregulated and 638 upregulated at P8 (**Fig. 5B, C**) (**Table 1**). As expected, we found many alterations associated with synaptic activity occurring at both stages retrieved by gene ontology (GO) analysis. Interestingly, among the GO Biological Processes terms specific for P4 we found *Chrdl1, Nlgn1, Dlg4* and *Shank3* that encode for Ventroptin, Neuroligin1, Dlg4 and Shank3 respectively and are all proteins essential for synapse formation and clusteing of AMPA receptos. However, at P8 we retrieved biological processes terms such as *Synaptic Assembly and Maintenance*, *Regulation of NMDA and AMPA Receptor Activity*, or *Transmission of Spontaneous Activity* that include several members of the Type I transmembrane AMPA receptors (Cacng2/4/7/8), Shisa8, involved in the regulation of AMPA receptors or Nrxn1, that is known to play a role in the formation and maintenance of synaptic juctions via their calcium dependent interactions with Neuroligin family members (**Fig. 5D**). Intringuingly, GO analysis of the genes specifically deregulated at P4 also retrieved some terms related to the regulation of the cell cycle.

Among the genes that were exclusively deregulated at P4 we found *Adcy1*, that encodes for Adenilate Cyclase 1, an enzyme known to be involved in the refinement of visual axons at the dLGN and the SC (Nicol et al., 2006). At P8, we found Sema3B that is known to play an important function in neuroplasticity regulation right after eye opening (Carulli et al., 2021). Among the highly downregulated genes that appeared at both stages we found Syt13, that encodes for Synaptotagmin 13, a type I membrane protein known to be involved in vesicular trafficking, exocytosis, and secretion (Fukuda and Mikoshiba, 2001; von Poser and Südhof, 2001) (**Fig. 5E**).

Since Syt13 was deregulated at both stages, we decided to manipulate the expression of this gene *in vivo* as a proof of concept to validate our screen. First, we analyzed the expression pattern of *Syt13 mRNA* by *in situ* hybridization in retinal sections from postnatal mice and confirmed that *Syt13* transcripts are highly and specifically expressed in P4 RGCs and still maintained although less expressed after eye opening (**Fig. 6A**). Then, to investigate the function of Syt13 in axon refinement, we electroporated short-hairpin RNAs against Syt13 (*shRNA Syt13*) or control shRNA together with plasmids encoding for the green fluorescence protein (GFP) into embryonic retinas (**Fig. 6B)**. The arborizations of targeted RGCs in the visual nuclei of electroporated mice at P10 were analyzed before eye-opening. GFP fluorescence completely filled the targeted neurons labeling the axonal arborizations at the SC. Most axons reached the corresponding topographical area at the SC in both control and *shRNA Syt13-expressing* RGCs. However, whereas control axons developed exuberant arborization in the target area, *shRNA Syt13-electroporated axons* showed significantly less dense arborizations (**Fig. 6C-D**). These results confirm a role for Syt13 in the refinement of RGC terminals at the SC and validates our unbiased screens designed to search for spontaneous activity-dependent molecules involved in axonal remodeling at the visual targets.

DISCUSSION

Spontaneous neural activity is essential in a multitude of processes in the developing nervous system. Spontaneous calcium transients have been detected in neocortex and thalamus in prenatal stages and may modulate neurogenesis wiring and neurotransmitter identity (Antón-Bolaños et al., 2019; Bonetti and Surace, 2010; Borodinsky et al., 2004; Corlew et al., 2004). In the visual system, correlated spontaneous retinal activity is known to be essential for the fine-tune of retinotopic maps and eye-specific segregation in the IFN, but it was unclear to what extent the

correct connectivity of RGC axons at NIFN also depend on activity correlation. In this study, by generating several mouse lines with disturbed correlated retinal activity before eye opening and analyzing the refinement of RGCs axon terminals in the SCN and the OPN, we found that activity correlation is essential for the establishement of proper connectivity also in NIFN. In addition, we retrieved the transcriptional programs triggered by correlated retinal activity essential for the proper assembly of the visual circuit.

Ectopic expression of Kir2.1 in RGCs alters correlated spontaneous activity

The rectifying potassium channel Kir2.1 is a known suppressor of intrinsic excitability, which has a crucial role in establishing the connectivity of several circuits. Overexpression of Kir2.1 has been used to electrically silence neurons in both *in vitro* and *in vivo* experiments (Burrone et al., 2002; Benjumeda et al., 2013). Moreover, ectopic expression of Kir2.1 in transgenic mice has been also reported to block neural activity in the olfactory system (Yu et al., 2004). However, ectopic expression of Kir2.1 may lead multiple and widely different effects in vivo, depending on the developmental stage of the network (Antón-Bolaños et al., 2019; Burrone et al., 2002). We observed that recombinant RGCs in the Kir2.1 mice exhibit a more negative resting potential than RGCs in the control mice. However, instead of being silenced, RGCs expressing Kir2.1 show a higher firing frequency. Thus, it appears that ectopic expression of Kir2.1 in RGCs at early embryonic stages leads to increased excitability rather than decreased or blocked activity. As a consequence, the whole set of RGCs do not fire in a correlated manner and this is sufficient to alter the refinement of retinal projections at the visual targets.

Particularities of retinal activity-dependent refinement in NIFN

A large number of studies have demonstrated that ipsilateral and contralateral axon terminals initially overlap in the dLGN and are later expelled from the territory that

corresponds to the other eye, competing with the contrary retinal input in terms of activity correlation. We observed eye-specific segregation defects in the IFN of the Slc6a4-Kir2.1 mice confirming that retinal activity is also altered in this mouse line. Mice in which glutamatergic activity was specifically abolished in ipsilaterally projecting RGCs (Slc6a4-cre; GlutV2) showed an increase in the contralateral but not in the ipsilateral territory (Koch et al., 2011). Here, using the same driver line, we impaired spontaneous activity in ipsilateral RGCs (iRGCs) before birth and observed that the area covered by ipsilateral axons is larger in the Kir2.1 mutants compared to the controls indicating that the refinement of ipsilateral RGCs depends on early spontaneous activity and revealing that early correlated spontaneous activity in these mice is essential to expel contralateral terminals from the ipsi-territory.

We shown here that when activity is altered, cRGCs terminals occupy the ipsilateral territory in a NIFN as the OPN. Therefore, despite the different anatomies of the IFN and NIFN, RGC terminals appear to follow similar rules to target and refine nuclei in terms of eye-specific activity competition. Despite eye-specific segregation does not take place in SCN, our experiments indicate that correlated retinal activity is also required for proper connectivity in this nuclei because Slc6a4-terminals innervate the ventrolateral quarter of the SCN, but their arbors are less restricted to this region and less densely organized in the Slc6a4-Kir2.1 mice. The SCN was thought to be just a regulator of the circadian clock. However, retinal input to the SCN encodes for a much more complex visual information than that necessary to just perform this function, suggesting a potential role for this nuclei in spatial vision as well (Mouland et al., 2017; Stinchcombe et al., 2017; Yu et al., 2017). Future experiments in conditional mice with altered retinal activity in all melanopsin-RGCs should better define the role of spontaneous activity in the refinement of retinal input to the SCN as well as its potential impact in mice behavior.

Transcriptional programs involved in activity-dependent axonal remodeling

Pou4f2-Kir2.1 mice show significant defects in fine-scale/local refinement of axonal arborizations at the different visual nuclei, confirming that the mechanisms involved in the remodeling of visual axons are influenced by correlated activity of neighboring RGCs. Therefore, to search for molecular programs activated by retinal activity correlation, we compared the transcriptomic profile of Pou4f2-Kir2.1 and control retinas. We analyzed two stages, P4, when axons are still remodeling and P8, when most axons are already refined and synaptic maturation is taking place. We found genes differentially expressed only in P4 or P8, likely reflecting the transcriptional changes associated to the transition of RGCs switching from a scenario dominated by axon branching dynamics to an assembled circuit carrying out synaptic maturation. Interestingly, Nlgn1, which is known to play an important role in recruiting and clustering other proteins during synaptogenesis is deregulated at P4 in the Kir2.1 mutants. Later, at P8 we also found Nrxn1, that is known to bind to Neuroligins form complexes at the synapses. At P4 we also found a number of DEGs related to cell cycle regulation when activity is altered. It has been recently reported that beyond its role in DNA damage response, the serin/threonine kinase ATR plays a function in regulating neuronal activity by modulating presynaptic firing. ATR interacts with synaptotagmins in synaptosomes and we found Synaptotagmin13, one of the less studied members of the synaptotagmin family (Wolfes and Dean, 2020), altered in the Kir2.1 mice. This could explain, at least partially, the *double-strand bread repair visa break-induced replication* GO terms that we retrieved in our analysis. In contrast to most members of this family, Syt13 does not sense calcium (Bhalla et al., 2008) but its downregulation leads to altered axonal arborizations at the SC. These results revealed a novel and important role for this poorly known member of the Syt family, but further experiments will be needed to precisely determine its function in the remodeling of RGC axon terminals as well as to characterize the function of other candidates retrieved in our screen.

MATERIALS AND METHODS

Mice

The Kir2.1eYFP$^{fl\text{-}Stop}$ line was generated in our laboratory by cloning the human Kir2.1 cDNA (Benjumeda et al., 2013) in a pEYFP-N1 plasmid adding the eYFP reporter protein at the C-terminal of Kir2.1. This fusion protein was subcloned in the PCAG-SE plasmid downstream of the CAG promoter and a LoxP-flanked STOP cassette. The function and plasma membrane localization of the chimeric channel were confirmed by electrophysiology. The linearized and purified construct was injected in mice oocytes (CEBATEG, Barcelona). Twelve funders were obtained and crossed with Pou4f2-cre mice (Dr. George Vann Bennet's laboratory in Duke University Medical Center) to select the funder with the higest Kir2.1YFP expression in RGCs. Slc6a4-cre line (Tg (Slc6a4-cre) ET33Gsat) belongs to the GENSAT Project at Rockefeller University (Stock Number: MMRC. 031028-UCD). Rosa26Stop-tdTm (B6.Cg-Gt(ROSA)26Sor$^{tm14(CAG\text{-}tdTomato)Hze}$/J) mice were acquired from Jackson Laboratories (Stock Number: 007914). Animals were housed in a timed-pregnancy breeding colony at the Instituto de Neurociencias de Alicante, Spain. Conditions and procedures were approved by the IN-Animal Care and Use Committee and met European (2013/63/UE) and Spanish regulations (RD 53/2013).

Electrophysiology

Retinas extracted from P4 or P11 (Pou4f2-cre::Kir2.1YFP^{fxStop}; R26^{Td}Tomato) and control (Kir2.1YFP^{fxStop}; R26^{Td}Tomato) mice were placed in artificial cerebrospinal fluid solution (ACSF) at 4 °C, containing (in mM): 126 mM NaCl, 26 mM $NaHCO_3$, 10 mM Glucose, 5 mM $MgCl_2$, 3 mM KCl, 1.25 mM NaH_2PO_4, 1 mM $CaCl_2$. pH of the ACSF solution was tampered using carbogen (5% CO2 and 95% oxygen) and the resulting osmolarity was ~310 mOsmol/Kg. Further, retinas were subjected to enzymatic digestion with collagenase/dispase diluted in ACSF (1:3) for 15-20 min at 35ºC with

carbogen. Collagenase/dispase mix was prepared as follow: 155 mM NaCl, 1.5 K_2PO_4, 10 mM HEPES, 5 mM glucose), collagenase type XI (Sigma, D9542) 900 uni/ml, dispase (BDBiosciences, 10103578.001) 5.5 uni/ml. Recordings were performed using a Olympus BX50WI up-right confocal microscope and constant perfusion with ACSF solution at ~34 ºC. Temperature was controlled by a feedback Peltier device CL-100 (Warner Instruments, Hamdem, CT, USA). Neurons were visualized through a 40x water immersion objective. To identify tdTm labeling, the field was expose to a 554 nm light with a Polychrome V monochromator (Thermo Scientific, USA) and the fluorescence emission captured on a cooled CCDge camera (sensicam, PCO AG, Kelheim, Germany). Whole-cell recordings were performed in current-clamp configuration using a Multiclamp 700B amplifier, pCLAMP 10 software and a Digidata 1440A and pCLAMP 10 software (Molecular Devices, Sunnyvale, USA). Borosilicate electrodes were pulled using a puller P-97 (Sutter Instrument, CA, USA) with resistance ranging between 4 to 8 MΩ and filled with an intracellular solution containing: 115 mM K-gluconate, 25 mM KCl, 9 mM NaCl, 10 mM HEPES, 0.2 mM EGTA, 1 mM $MgCl_2$, 3 mM K_2-ATP and 1 mM Na-GTP adjusted to pH 7.2 with KOH (280–290 mOsmol/kg). TdTm-cells were selected and held at -60 mV for few seconds. Further, we recorded responses at resting membrane potential for 5-9 min. Data were sampled at a frequency of 20 KHz and low-passed filtered at 10 KHz. Firing frequency (events or bursts per minute) was measured and the firing patterns were classified as tonic/train, bursts, oscillations/events or no responses (NR). The data were analyzed using the Clampex 10.1 software (Molecular Devices Corp., Sunnyvale, CA, USA). Statistical analyses were performed with SigmaStat 4.0 software (Systat Software) and Origin Pro8 software (OriginLab Corporation) was used for graphing. Data are reported as the mean ± SEM. Significance was set as *$p < 0.05$, ** $p<0.01$ and *** $p<0.001$ as assessed by Student's t-test.

Anterograde labeling of retinal projections

Postnatal mice were anaesthetized in ice or with isofluorane depending on the age. Whole-eye anterograde labelling was performed using a *Nanoject II Auto-Nanoliter Injector (Drummond, 3-000-204)* injecting twice on opposite points with 0.5µl of CTB-subunit conjugated with Alexa Fluor 488 or 647 *(Invitrogen, C34775/C22843/C34778) as* described in (Rebsam et al., 2009). Two days later mice were perfused transcardially with 4% paraformaldehyde (PFA) in 0.1 M phosphate-buffered saline (PBS). Brains were incubated overnight in the PFA solution at 4ºC and stored in PBS. Fixed tissue was embedded in 3% agarose diluted in PBS and sectioned in a vibratome. Sections were incubated in blocking solution (0.2% gelatin, 5% FBS, 0.005-0.01% Tx) at RT for 1h and mounted to be analyzed.

Inmunofluorescence and in situ hybridization

Sectioned PFA fixed tissue was incubated in blocking solution (0.2% gelatin, 5% FBS, 0.005-0.01% Tx) at RT for 1h, followed by incubation O/N with the primary antibodies. The next primary antibodies were used at the specified concentrations: rabbit anti-Dsred Pab (Clontech, 632496) (1:500), rabbit polyclonal Kir2.1 (Abcam, ab65796) (1:500), chicken anti-GFP (Aves Lab, GFP-1020) (1:1000), rabbit polyclonal anti-melanopsin (Advanced targeting systems, AB-N38) (1:2500). After three washes in PBS, samples were incubated with the secondary antibodies diluted 1:1000 in blocking solution at room temperature for 2 h. For whole-mount retinas, the protocol was the same used for sections but Triton concentration was increased to 1% and samples were fixated in methanol. This process includes washes with 25%-50%-80%-100% methanol/H2O for 20' at RT, a bleaching in 3% H2O2 in methanol for 1h at RT, two washes in methanol, rehydration in 80%-50%-25% methanol/PBS 20' each at RT and blocking in 5% BSA PBST (3% Tween) for 1 hour at RT. In situ hybridization for *mRNA Syt13* was performed in P4 retinal cryosections and combined with anti- Pou4f2 antibodies (Chemicon).

Brain clarification

Clarification was performed following the iDISCO protocol (Renier et al., 2014). Briefly, samples were dehydrated in methanol/H2O series (20%-40%-60%-80%-100%-100%) 1h at RT. Then samples were incubated 3h, with shaking, in 66% DCM/methanol at RT, and washed in 100% DCM to wash the methanol. Finally, brains were incubated and storaged in a glass tube totally filled with DiBenzylEther at RT. Brains showing total filling of contralateral projections labelled with CTB-546 and ipsilateral with CTB-647 were selected. For 3D quantifications, dLGN stacks were previously transformed to IsoData binary masks in ImageJIsoData algorithm) to standardize rendering in Imaris.

Image acquisition and analysis

Images from tissue sections were captured using Olympus FV1000 confocal IX81 microscope and FV10-ASW software (Olympus). Acquisitions from clarified brains were made using a Light Sheet microscope (LaVision Ultramicroscope II) and LaVision BioTec Inspector Pro (LaVision). 3D rendering and processing were carried out in Imaris 9.1.2 (Bitplane). Images were processed in the ImageJ distribution Fiji (Schindelin et al., 2012) in order to denoise, enhance, threshold, co-localize or measure areas and distances, depending on the type of quantification. In all cases, background fluorescence was subtracted from sections using a rolling ball filter and gray scale was renormalized so that the range of gray-scale values was from 0 to 256. Data obtained from the image analysis were loaded into R 3.6.0 (R Core Team 2019) to perform mathematical calculations and generate some of the graphs. Statistical analysis and the rest of graphs were carried out using GrapPhad Prism version 6.00 (GraphPad Software). Figures and graphs were edited with Adobe Illustrator CS6 (Adobe Systems Inc.). Error bars indicate ± SEM. (**$p < 0.01$, ***$p < 0.001$, Student's unpaired t test).

Analysis of axon terminals ocupancy in the superior colliculus of electroporated mice

A region of interest (ROI) was drawn around the superior colliculus. Minimum and maximum threshold values were used to select the pixels belonging to GFP axons in the ROI of each section. The area occupied by GFP axons was expressed as the percentage of the total area of the superior colliculus. We call this value the “GFP-covered Area".

Eye-specific segregation analysis

Binocular co-localization was computed overlapping the “IsoData” binary mask of the Z-stack for each channel. We selected the two (OPN, SCN) or three (dLGN) most central 70-micron sections from the nucleus. The result was normalized by the total area of the nucleus. R-distribution was carried out as described in Torborg, et al. (Torborg and Feller, 2004) computing the logarithm of the intensity ratio ($R = log_{10}(F_I/F_C)$). The intensity threshold was set at 5 and empty pixels in both channels were discarded. The remaining zero-value pixels were replaced by 0.01 to allow the calculation of the logarithm. Range [-0.5, +0.5] was considered non-segregated area and [+1.75, +2.5] as ipsidominant area. The ipsilateral territory was obtained by comparing the pixels with ipsilateral signal to the total number of pixels of the dLGN.

Suprachiasmatic nucleus density and proximity analysis

All 60-micron coronal sections of the SCN were analyzed, being aggregated by sample and averaged by group. TdTm pixels co-localizing with both Alexa fluorophores were discarded because of the inability to assign them to a specific retinal input. For the ipsilateral/contralateral proximity analysis, regions with high CTB-Alx accumulation were selected as an approximation to synaptic boutons. Ipsilateral boutons are those labeled by the corresponding CTB-Alx conjugate and tdTm. Contralateral boutons are

those positive for the other CTB-Alx conjugate from the lacking tdTm signal. In the computation of the density maps, the sum of the two sides of the nucleus was considered as the total signal. In addition, both channels were averaged and nucleus size and signal intensity was normalized prior to grouping the samples.

In utero electroporation

In utero electroporation was performed as in Morenilla-Palao et al. (Morenilla-Palao et al., 2020) and sections of the SC of P11 electroporated mice were obtained and visualized as in (Benjumeda et al., 2013)***.***

RNA-seq and analysis

Retinas were dissected out from P4 Pou4f2-cre; R26^{Td}Tomato (control RGCs) and Pou4f2-Kir2.1; R26^{Td}Tomato (Kir2.1 RGCs) mice. Isolated retinas were enzymatically dissociated in a mixture of collagenase/Trypsin and 1% BSA for 20 minutes at 37.C followed by mechanical dissociation. A 40 µM cell strainer was used for aggregates removal after dissociation and TdTm-expressing RGCs were isolated by fluorescent-activated cell sorting (BD FACS Aria™ III. BD Bioscience). Total RNA extraction was performed with Arcturus Picopure RNA isolation Kit (ThermoFisher Scientific). Three independent samples containing total RNA from 9-11 pooled retinas from at least three different litters/condition were sequenced according to the manufacturer instructions in a HiSeq Sequencing v4 Chemistry (Illumina, Inc). Briefly, RNAseq reads were mapped to the mouse genome (Mus_musculus.GRCm.38.83) using STAR (v2.5.0c) (Dobin et al., 2013). Quality control of the raw data was performed with FastQC (http://www.bioinformatics.babraham.ac.uk/projects/fastqc/). Library sizes were between 17 and 23 million single reads. Samtools (v1.3.1) was used to handle BAM files (Li et al., 2009). To retrieve differentially expressed genes (DEG), mapped reads were counted with HTSeq v0.6.1 (Anders et al., 2015) with the following parameters: -s reverse --i gene_id and with a gtf file reference for GRCm38.83. Samples were

adjusted for library size and normalized with the variance stabilizing transformation (vst) in the R statistical environment using DESeq2 (v1.10.0) pipeline (Love et al., 2014). When performing differential expression analysis between groups, we applied the embedded IndependentFiltering procedure to exclude genes that were not expressed at appreciable levels in most of the samples. A heatmap of this distance matrix gives us an overview over similarities and dissimilarities between samples with a clustering based on the distances between the rows/columns of the distance matrix (FigS4). The PCA is generates using the most variable genes detected in the entire dataset. DESeq2 default values are set to use only the 500 most variable genes. This number is often applied when transcription of protein-coding genes is analysed (FigS4). Gene expression values were represented using the normalization techniques provided by each algorithm: *Reads per Kilobase of Mapped reads* (RPKM), *Relative Log Expression* (rlog from *DESeq2*). Analysis and preprocessing of data were performed with custom scripts using R (https://cran.r-project.org/) (v3.4.3) statistical computing and graphics, and bioconductor v3.2 (BiocInstaller 1.20.3) (Huber et al., 2015). Genes were considered differentially expressed at Benjamini–Hochberg (BH) adjusted, Padj < 0.1 and abs|Log2FC| > 1. Significantly upregulated and downregulated genes were visualized with IGV (v2.3.72) (Thorvaldsdóttir et al., 2013). We performed an Enrichment Analysis for Gene Ontology using the platform Panther (Mi et al., 2019) Fisher's exact test and the Padj correction were used, obtaining the top terms using the filters by ratio enrichment > 2, number of GO family group genes between 3 and 2000, number of enrichment genes >3.

Sample	N.of reads	Type of Sequencing	Read length
WT4A	20336665	RNAseq	50
WT4B	17037440	RNAseq	50
KI4A	20486888	RNAseq	50

KI4B	22784329	RNAseq	50
KI4C	22014785	RNAseq	50
WT8A	17011088	RNAseq	50
WT8B	21874606	RNAseq	50
KI8A	19331263	RNAseq	50
KI8B	18924756	RNAseq	50
KI8C	16368599	RNAseq	50

Datasets can be accessed at the GEO repository (GSE193498).

Go to https://www.ncbi.nlm.nih. Enter token **ynirkwgshryzlkt** into the box

ACKNOWLEDGMENTS

The laboratory of EH is funded with the following grants: PID2019-110535GB-I00 from the National Grant Research Program, PROMETEO Program (PROMETEO/2020/007) from Generalitat Valenciana, 20191956 from the Ramón Areces Foundation, a ERC-282329 grant from the European Research Council. The laboratory of AG is funded by PID2019-108194RB-100 from the National Grant Research Program. We also acknowledge the financial support received from the “Severo Ochoa” Program for Centers of Excellence in R&D (SEV-2017-0723).

STATEMENT OF COMPETING INTERESTS

All authors declare that they have no competing interests.

AUTHOR CONTRIBUTIONS

SN performed and analyzed the CTB-tracing experiments. C M-P generated the Kir2.1 transgenic mice and extracted retinal RNA for RNA-seq experiments. MH performed in situ hybridization and *in utero* electroporation experiments. MT L-C performed the computational analysis of RNA-seq data. DF perfomed electrophysiology experiments and AG analyzed the electrophysiology data. EH and SN wrote the original draft and EH designed, conceived and supervised the study.

BIBLIOGRAPHY:

Anders S, Pyl PT, Huber W. 2015. HTSeq--a Python framework to work with high-throughput sequencing data. *Bioinformatics* **31**:166–9. doi:10.1093/bioinformatics/btu638

Antón-Bolaños N, Sempere-Ferràndez A, Guillamón-Vivancos T, Martini FJ, Pérez-Saiz L, Gezelius H, Filipchuk A, Valdeolmillos M, López-Bendito G. 2019. Prenatal activity from thalamic neurons governs the emergence of functional cortical maps in mice. *Science* **364**:987–990. doi:10.1126/science.aav7617

Benjumeda I, Escalante A, Law C, Morales D, Chauvin G, Muça G, Coca Y, Márquez J, López-Bendito G, Kania A, Martínez L, Herrera E. 2013. Uncoupling of EphA/ephrinA signaling and spontaneous activity in neural circuit wiring. *J Neurosci* **33**:18208–18. doi:10.1523/JNEUROSCI.1931-13.2013

Berson DM, Dunn FA, Takao M. 2002. Phototransduction by retinal ganglion cells that set the circadian clock. *Science* **295**:1070–3. doi:10.1126/science.1067262

Bhalla A, Chicka MC, Chapman ER. 2008. Analysis of the synaptotagmin family during reconstituted membrane fusion. Uncovering a class of inhibitory isoforms. *J Biol Chem* **283**:21799–807. doi:10.1074/jbc.M709628200

Bito H, Deisseroth K, Tsien RW. 1997. Ca2+-dependent regulation in neuronal gene expression. *Curr Opin Neurobiol* **7**:419–29. doi:10.1016/s0959-4388(97)80072-4

Bonetti C, Surace EM. 2010. Mouse embryonic retina delivers information controlling cortical neurogenesis. *PLoS One* **5**:e15211. doi:10.1371/journal.pone.0015211

Borodinsky LN, Root CM, Cronin JA, Sann SB, Gu X, Spitzer NC. 2004. Activity-dependent homeostatic specification of transmitter expression in embryonic neurons. *Nature* **429**:523–30. doi:10.1038/nature02518

Burrone J, Byrne MO, Murthy VN. 2002. Multiple forms of synaptic plasticity triggered by selective suppression of activity in individual neurons **420**. doi:10.1038/nature01179.1.

Carulli D, de Winter F, Verhaagen J. 2021. Semaphorins in Adult Nervous System Plasticity and Disease. *Front Synaptic Neurosci* **13**:672891. doi:10.3389/fnsyn.2021.672891

Chalupa LM, Snider CJ. 1998. Topographic specificity in the retinocollicular projection of the developing ferret: an anterograde tracing study. *J Comp Neurol* **392**:35–47.

Chen SK, Badea TC, Hattar S. 2011. Photoentrainment and pupillary light reflex are mediated by distinct populations of ipRGCs. *Nature* **476**:92–96. doi:10.1038/nature10206

Corlew R, Bosma MM, Moody WJ. 2004. Spontaneous, synchronous electrical activity

in neonatal mouse cortical neurones. *J Physiol* **560**:377–90. doi:10.1113/jphysiol.2004.071621

Demas J, Eglen SJ, Wong ROL. 2003. Developmental loss of synchronous spontaneous activity in the mouse retina is independent of visual experience. *J Neurosci* **23**:2851–2860. doi:23/7/2851 [pii]

Dhande OS, Estevez ME, Quattrochi LE, El-Danaf RN, Nguyen PL, Berson DM, Huberman AD. 2013. Genetic dissection of retinal inputs to brainstem nuclei controlling image stabilization. *J Neurosci* **33**:17797–813. doi:10.1523/JNEUROSCI.2778-13.2013

Do MTH, Yau K-W. 2010. Intrinsically photosensitive retinal ganglion cells. *Physiol Rev* **90**:1547–81. doi:10.1152/physrev.00013.2010

Dobin A, Davis CA, Schlesinger F, Drenkow J, Zaleski C, Jha S, Batut P, Chaisson M, Gingeras TR. 2013. STAR: ultrafast universal RNA-seq aligner. *Bioinformatics* **29**:15–21. doi:10.1093/bioinformatics/bts635

Fernandez DC, Chang Y-T, Hattar S, Chen S-K. 2016. Architecture of retinal projections to the central circadian pacemaker. *Proc Natl Acad Sci* **113**:6047–6052. doi:10.1073/pnas.1523629113

Fuerst PG, Bruce F, Rounds RP, Erskine L, Burgess RW. 2012. Cell autonomy of DSCAM function in retinal development. *Dev Biol* **361**:326–37. doi:10.1016/j.ydbio.2011.10.028

Fukuda M, Mikoshiba K. 2001. Characterization of KIAA1427 protein as an atypical synaptotagmin (Syt XIII). *Biochem J* **354**:249–57. doi:10.1042/0264-6021:3540249

Galli L, Maffei L. 1988. Spontaneous impulse activity of rat retinal ganglion cells in prenatal life. *Science* **242**:90–1. doi:10.1126/science.3175637

Gamlin PDR. 2006. The pretectum: connections and oculomotor-related roles. *Prog Brain Res* **151**:379–405. doi:10.1016/S0079-6123(05)51012-4

García-Frigola C, Herrera E. 2010. Zic2 regulates the expression of Sert to modulate eye-specific refinement at the visual targets. *EMBO J* **29**:3170–83. doi:10.1038/emboj.2010.172

Godement P, Salaün J, Imbert M. 1984. Prenatal and postnatal development of retinogeniculate and retinocollicular projections in the mouse. *J Comp Neurol* **230**:552–75. doi:10.1002/cne.902300406

Hattar S, Liao HW, Takao M, Berson DM, Yau KW. 2002. Melanopsin-containing retinal ganglion cells: architecture, projections, and intrinsic photosensitivity. *Science* **295**:1065–70. doi:10.1126/science.1069609

Hattar S, Lucas RJ, Mrosovsky N, Thompson S, Douglas RH, Hankins MW, Lem J, Biel M, Hofmann F, Foster RG, Yau K-W. 2003. Melanopsin and rod-cone

photoreceptive systems account for all major accessory visual functions in mice. *Nature* **424**:76–81. doi:10.1038/nature01761

Huber W, Carey VJ, Gentleman R, Anders S, Carlson M, Carvalho BS, Bravo HC, Davis S, Gatto L, Girke T, Gottardo R, Hahne F, Hansen KD, Irizarry RA, Lawrence M, Love MI, MacDonald J, Obenchain V, Oleś AK, Pagès H, Reyes A, Shannon P, Smyth GK, Tenenbaum D, Waldron L, Morgan M. 2015. Orchestrating high-throughput genomic analysis with Bioconductor. *Nat Methods* **12**:115–21. doi:10.1038/nmeth.3252

Kato I, Harada K, Hasegawa T, Igarashi T, Koike Y, Kawasaki T. 1986. Role of the nucleus of the optic tract in monkeys in relation to optokinetic nystagmus. *Brain Res* **364**:12–22. doi:10.1016/0006-8993(86)90982-0

Koch SM, Dela Cruz CG, Hnasko TS, Edwards RH, Huberman AD, Ullian EM. 2011. Pathway-specific genetic attenuation of glutamate release alters select features of competition-based visual circuit refinement. *Neuron* **71**:235–42. doi:10.1016/j.neuron.2011.05.045

Li H, Handsaker B, Wysoker A, Fennell T, Ruan J, Homer N, Marth G, Abecasis G, Durbin R, 1000 Genome Project Data Processing Subgroup. 2009. The Sequence Alignment/Map format and SAMtools. *Bioinformatics* **25**:2078–9. doi:10.1093/bioinformatics/btp352

Love MI, Huber W, Anders S. 2014. Moderated estimation of fold change and dispersion for RNA-seq data with DESeq2. *Genome Biol* **15**:550. doi:10.1186/s13059-014-0550-8

Marcucci F, Murcia-Belmonte V, Wang Q, Coca Y, Ferreiro-Galve S, Kuwajima T, Khalid S, Ross ME, Mason C, Herrera E. 2016. The Ciliary Margin Zone of the Mammalian Retina Generates Retinal Ganglion Cells. *Cell Rep* **17**:3153–3164. doi:10.1016/j.celrep.2016.11.016

McLaughlin T, Hindges R, O'Leary DD. 2003. Regulation of axial patterning of the retina and its topographic mapping in the brain. *Curr Opin Neurobiol* **13**:57–69. doi:10.1016/S0959-4388(03)00014-X

Mi H, Muruganujan A, Huang X, Ebert D, Mills C, Guo X, Thomas PD. 2019. Protocol Update for large-scale genome and gene function analysis with the PANTHER classification system (v.14.0). *Nat Protoc* **14**:703–721. doi:10.1038/s41596-019-0128-8

Morenilla-Palao C, López-Cascales MT, López-Atalaya JP, Baeza D, Calvo-Díaz L, Barco A, Herrera E. 2020. A Zic2-regulated switch in a noncanonical Wnt/βcatenin pathway is essential for the formation of bilateral circuits. *Sci Adv* **6**. doi:10.1126/sciadv.aaz8797

Mouland JW, Stinchcombe AR, Forger DB, Brown TM, Lucas RJ. 2017. Responses to Spatial Contrast in the Mouse Suprachiasmatic Nuclei. *Curr Biol* **27**:1633-1640.e3. doi:10.1016/j.cub.2017.04.039

Nakamoto C, Durward E, Horie M, Nakamoto M. 2019. Nell2 regulates the contralateral-versus-ipsilateral visual projection as a domain-specific positional cue. *Development* **146**. doi:10.1242/dev.170704

Nicol X, Muzerelle A, Rio JP, Métin C, Gaspar P. 2006. Requirement of adenylate cyclase 1 for the ephrin-A5-dependent retraction of exuberant retinal axons. *J Neurosci* **26**:862–72. doi:10.1523/JNEUROSCI.3385-05.2006

Noseda R, Burstein R. 2011. Advances in understanding the mechanisms of migraine-type photophobia. *Curr Opin Neurol* **24**:197–202. doi:10.1097/WCO.0b013e3283466c8e

Pak W, Hindges R, Lim Y, Pfaff SL, Leary DDMO. 2004. Magnitude of Binocular Vision Controlled by Islet-2 Repression of a Genetic Program that Specifies Laterality of Retinal Axon Pathfinding **119**:567–578.

Pham TA, Rubenstein JL, Silva AJ, Storm DR, Stryker MP. 2001. The CRE/CREB pathway is transiently expressed in thalamic circuit development and contributes to refinement of retinogeniculate axons. *Neuron* **31**:409–20.

Prigge CL, Yeh P-T, Liou N-F, Lee C-C, You S-F, Liu L-L, McNeill DS, Chew KS, Hattar S, Chen S-K, Zhang D-Q. 2016. M1 ipRGCs Influence Visual Function through Retrograde Signaling in the Retina. *J Neurosci* **36**:7184–97. doi:10.1523/JNEUROSCI.3500-15.2016

Rakic P. 1976. Prenatal genesis of connections subserving ocular dominance in the rhesus monkey. *Nature* **261**:467–71. doi:10.1038/261467a0

Rebsam A, Petros TJ, Mason CA. 2009. Switching retinogeniculate axon laterality leads to normal targeting but abnormal eye-specific segregation that is activity dependent. *J Neurosci* **29**:14855–14863. doi:10.1523/JNEUROSCI.3462-09.2009

Renier N, Wu Z, Simon DJ, Yang J, Ariel P, Tessier-lavigne M. 2014. Resource iDISCO□: A Simple , Rapid Method to Immunolabel Large Tissue Samples for Volume Imaging. *Cell* **159**:896–910. doi:10.1016/j.cell.2014.10.010

Renna JM, Weng S, Berson DM. 2011. Light acts through melanopsin to alter retinal waves and segregation of retinogeniculate afferents. *Nat Neurosci* **14**:827.

Schindelin J, Arganda-Carreras I, Frise E, Kaynig V, Longair M, Pietzsch T, Preibisch S, Rueden C, Saalfeld S, Schmid B, Tinevez JY, White DJ, Hartenstein V, Eliceiri K, Tomancak P, Cardona A. 2012. Fiji: An open-source platform for biological-image analysis. *Nat Methods* **9**:676–682. doi:10.1038/nmeth.2019

Schmidt TM, Kofuji P. 2011. Structure and function of bistratified intrinsically

photosensitive retinal ganglion cells in the mouse. *J Comp Neurol* **519**:1492–504. doi:10.1002/cne.22579

Sekaran S, Foster RG, Lucas RJ, Hankins MW. 2003. Calcium imaging reveals a network of intrinsically light-sensitive inner-retinal neurons. *Curr Biol* **13**:1290–8. doi:10.1016/s0960-9822(03)00510-4

Sekaran S, Lupi D, Jones SL, Sheely CJ, Hattar S, Yau K-W, Lucas RJ, Foster RG, Hankins MW. 2005. Melanopsin-dependent photoreception provides earliest light detection in the mammalian retina. *Curr Biol* **15**:1099–107. doi:10.1016/j.cub.2005.05.053

Sernagor E. 2005. Retinal development: second sight comes first. *Curr Biol* **15**:R556-9. doi:10.1016/j.cub.2005.07.004

Stinchcombe AR, Mouland JW, Wong KY, Lucas RJ, Forger DB. 2017. Multiplexing Visual Signals in the Suprachiasmatic Nuclei. *Cell Rep* **21**:1418–1425. doi:10.1016/j.celrep.2017.10.045

Stryker MP, Schiller PH. 1975. Eye and head movements evoked by electrical stimulation of monkey superior colliculus. *Exp brain Res* **23**:103–12. doi:10.1007/bf00238733

Su J, Sabbagh U, Liang Y, Olejníková L, Dixon KG, Russell AL, Chen J, Pan YA, Triplett JW, Fox MA. 2021. A cell-ECM mechanism for connecting the ipsilateral eye to the brain. *Proc Natl Acad Sci U S A* **118**. doi:10.1073/pnas.2104343118

Thorvaldsdóttir H, Robinson JT, Mesirov JP. 2013. Integrative Genomics Viewer (IGV): high-performance genomics data visualization and exploration. *Brief Bioinform* **14**:178–92. doi:10.1093/bib/bbs017

Torborg CL, Feller MB. 2005. Spontaneous patterned retinal activity and the refinement of retinal projections. *Prog Neurobiol* **76**:213–35. doi:10.1016/j.pneurobio.2005.09.002

Torborg CL, Feller MB. 2004. Unbiased analysis of bulk axonal segregation patterns. *J Neurosci Methods* **135**:17–26. doi:10.1016/j.jneumeth.2003.11.019

Torborg CL, Hansen KA, Feller MB. 2005. High frequency, synchronized bursting drives eye-specific segregation of retinogeniculate projections. *Nat Neurosci* **8**:72–8. doi:10.1038/nn1376

Upton AL, Salichon N, Lebrand C, Ravary A, Blakely R, Seif I, Gaspar P. 1999. Excess of serotonin (5-HT) alters the segregation of ispilateral and contralateral retinal projections in monoamine oxidase A knock-out mice: possible role of 5-HT uptake in retinal ganglion cells during development. *J Neurosci* **19**:7007–24.

von Poser C, Südhof TC. 2001. Synaptotagmin 13: structure and expression of a novel synaptotagmin. *Eur J Cell Biol* **80**:41–7. doi:10.1078/0171-9335-00133

West AE, Chen WG, Dalva MB, Dolmetsch RE, Kornhauser JM, Shaywitz AJ, Takasu MA, Tao X, Greenberg ME. 2001. Calcium regulation of neuronal gene expression. *Proc Natl Acad Sci U S A* **98**:11024–31. doi:10.1073/pnas.191352298

Wolfes AC, Dean C. 2020. The diversity of synaptotagmin isoforms. *Curr Opin Neurobiol* **63**:198–209. doi:10.1016/j.conb.2020.04.006

Wong RO, Meister M, Shatz CJ. 1993. Transient period of correlated bursting activity during development of the mammalian retina. *Neuron* **11**:923–38.

Yonehara K, Ishikane H, Sakuta H, Shintani T, Nakamura-Yonehara K, Kamiji NL, Usui S, Noda M. 2009. Identification of retinal ganglion cells and their projections involved in central transmission of information about upward and downward image motion. *PLoS One* **4**:e4320. doi:10.1371/journal.pone.0004320

Young MJ, Lund RD. 1994. The anatomical substrates subserving the pupillary light reflex in rats: origin of the consensual pupillary response. *Neuroscience* **62**:481–96. doi:10.1016/0306-4522(94)90381-6

Yu CR, Power J, Barnea G, O'Donnell S, Brown HEV, Osborne J, Axel R, Gogos JA. 2004. Spontaneous neural activity is required for the establishment and maintenance of the olfactory sensory map. *Neuron* **42**:553–566. doi:10.1016/S0896-6273(04)00224-7

Yu Y-Q, Barry DM, Hao Y, Liu X-T, Chen Z-F. 2017. Molecular and neural basis of contagious itch behavior in mice. *Science* **355**:1072–1076. doi:10.1126/science.aak9748

FIGURE LEGENDS

Figure 1. Kir2.1eYFP$^{fl\text{-}Stop}$ mouse express Kir2.1 in RGCs leading to altered retinal waves. (A) Generation of the Pou4f2-Kir2.1 mouse line. The Pou4f2-cre mice were breed with a conditional reporter line that contains a CAG-[Stop] cassette followed by the human Kir2.1 cDNA sequence fused to the eYFP coding sequence. **(B)** Immunostaining for Kir2.1 and YFP in retinal sections from adult Pou4f2-Kir2.1 and control littermate mice. Panels at the bottom show expression of Kir2.1 alone or combined with Calretinin in Pou4f2-Kir2.1 mouse retinas. **(C)** Averaged resting membrane potential in control cells and cells expressing Kir2.1. **(D)** Examples of neurons from control and Pou4f2-Kir2.1 mice at P11 and P4 recorded in whole cell current clamp configuration. **(E)** Pie graphs despiting the number of cells showing the different electrophysiological patterns. **(F)** Firing frequency distinguishing between events and bursts from control (n= 11) and Pou4f2-Kir2.1 (n= 12) cells. Error bars indicate ±SEM (*$p < 0.05$, Student's unpaired T-test).

Figure 2. Pou4f2-Kir2.1 mice have eye specific segregation defects in the dLGN. (A) Retinal projections were labeled through intraocular injections of cholera toxin subunit B conjugated to different Alexa fluorophores (CTB-Alx647 and CTB-Alx488) for each eye. **(B, C)** 3D reconstructions and **(D-E)** coronal sections through the dLGN of P11 Pou4f2-Kir2.1 and control littermate mice injected with CTB-Alx647 and CTB-Alx488. Overlaping of ipsilateral and contralateral terminals is visualized in white. **(D'-E')** R-distribution (log[ipsilateral/contralateral]) representing contralateral dominant area in red, unsegregated in green and ipsilateral dominant in blue. **(F)** Unsegregated area [-0.5,0.5] and **(G)** ipsi-dominant area [1.75, 2.5] were obtained from the R distribution. **(H)** dLGN area occupied by ipsilateral projections. Each biological replicate (red dots) was obtained by averaging the results for the three central sections of one of the nuclei. Error bars indicate ±SEM (***$p < 0.001$, Student's unpaired T-test).

Figure 3. OPN requires organized spontaneous retinal activity to refine and elicit eye-specific segregation. (A) Retinal projections were labeled through intraocular injections of cholera toxin subunit B fused to different Alexa fluorophores (CTB-Alx647 and CTB-Alx488) for each eye. **(B-C)** 3D reconstructions and **(D-E)** coronal sections through the OPN of P11 Pou4f2-Kir2.1 and control littermate mice injected with CTB-Alx647 and CTB-Alx488. Overlaping of ipsilateral and contralateral terminals is visualized in white. **(F)** Ratio of overlapping between contralateral and ipsilateral projections. Each biological replicate (red dots) was obtained by averaging the results for the two central sections of one of the nuclei. Error bars indicate ±SEM (***$p < 0.001$, Student's unpaired T-test).

Figure 4. Correlated retinal activity is needed for the refinement of visual axons in the SCN. (A-A') Whole-mount retina from P11 Slc6a4-TdTm mice stained with αOPN4 and αtdTomato antibodies. Yellow arrowheads point to double stained cells. **(B)** Scheme illustrating the experimental approach. Monocular injection of CTB fused to Alexa-488 in Slc6a4-Kir2.1 or control mice and analysis of coronal sections at the level of the SCN (yellow) two days later. Retinal projections from each eye bilaterally innervate the SCN **(C)** Heatmaps displaying projections from the ipsilateral RGCs to the SCN in Slc6a4-Kir2.1 and control mice, obtained by averaging all the replicates per condition. Percentages indicate the ratio of ipsilateral RGC innervation to each side of the SCN. **(D)** Ratio of the ipsilateral projections located in the ventrolateral SCN (dashed rectangle in C). Each biological replicate (red dots in D) was obtained by summing the binary mask for each Z-plane along all sections of the SCN, and averaging the input from both eyes (different CTB-Alx conjugates). The images were then scaled to normalize by nucleus size and obtain comparable density maps. Error bars indicate ±SEM (***$p < 0.001$, Student's unpaired T-test).

Figure 5. Activity-dependent transcriptional program that contol axon remodeling.

(A) Scheme of the experimental approach. RGCs from P4 Pou4f2-Kir2.1 and control littermate mice were purified by FACS and their total RNA extracted to compare their transciptomic profiles. **(B)** Heatmaps of gene transcriptional profiles of RGCs from Pou4f2-Kir2.1 and control mice highlighting common and specific DEGs at P4 and P8. **(C)** Volcano plots showing the significance value distribution after DEGs analysis between Pou4f2-Kir2.1 and control mice at P4 and P8 (Padj < 0.1); |LFC|>1 = 217 genes. **(D)** Heatmaps of upregulated and downregulated DEGs in P4, P8 or common to both stages comparing Pou4f2-cre-Kir2.1 and control retinas. **(E)** Biological processes GO enrichment analysis of DEGs from genes with altered expression in P4, P8 or both in Pou4f2-cre-Kir2.1 mice compared to controls. P.adj < 0.1. **(F)** Gene profiles and graphs representing transcripts expression obtained in Pou4f2-Kir2.1 and control mice corresponding to three DEGs, *Adcy1*, Sema6a and *Syt13* at both stages.

Figure 6. Syt13 is essential for axon refinement at the visual targets. (A) *In situ* hybridization for Syt13 in retinal sections from P4 and P15 wildtype mice (left panels) combined with inmnohistochemistry for the RGC marker Pou4f2 and DAPI (right panels). GCl, Ganglion cell layer, INl, Inner layer, ONl, outer layer. **(B)** Schematic representation of the experimental approach. **(C)** Representative examples of sagittal sections through the Superior Colliculus (SC) of P11 mice electroporated at E13 with plasmids encoding for GFP and control shRNA or Syt13shRNA and contrastained with DAPI. Righ panels (i, ii) show high magnification images from the squared areas. **(D)** Fluorescence intensity from axons of RGCs targeted at E13 by electroporation measured in sagittal sections at the SC level and normalized to the total area occupied by the SC in each slide. Analyzed slides (grey dots) come from three different mice (Student's unpaired T-test, ***pvalue < 0.001). Results show means ± SEM.

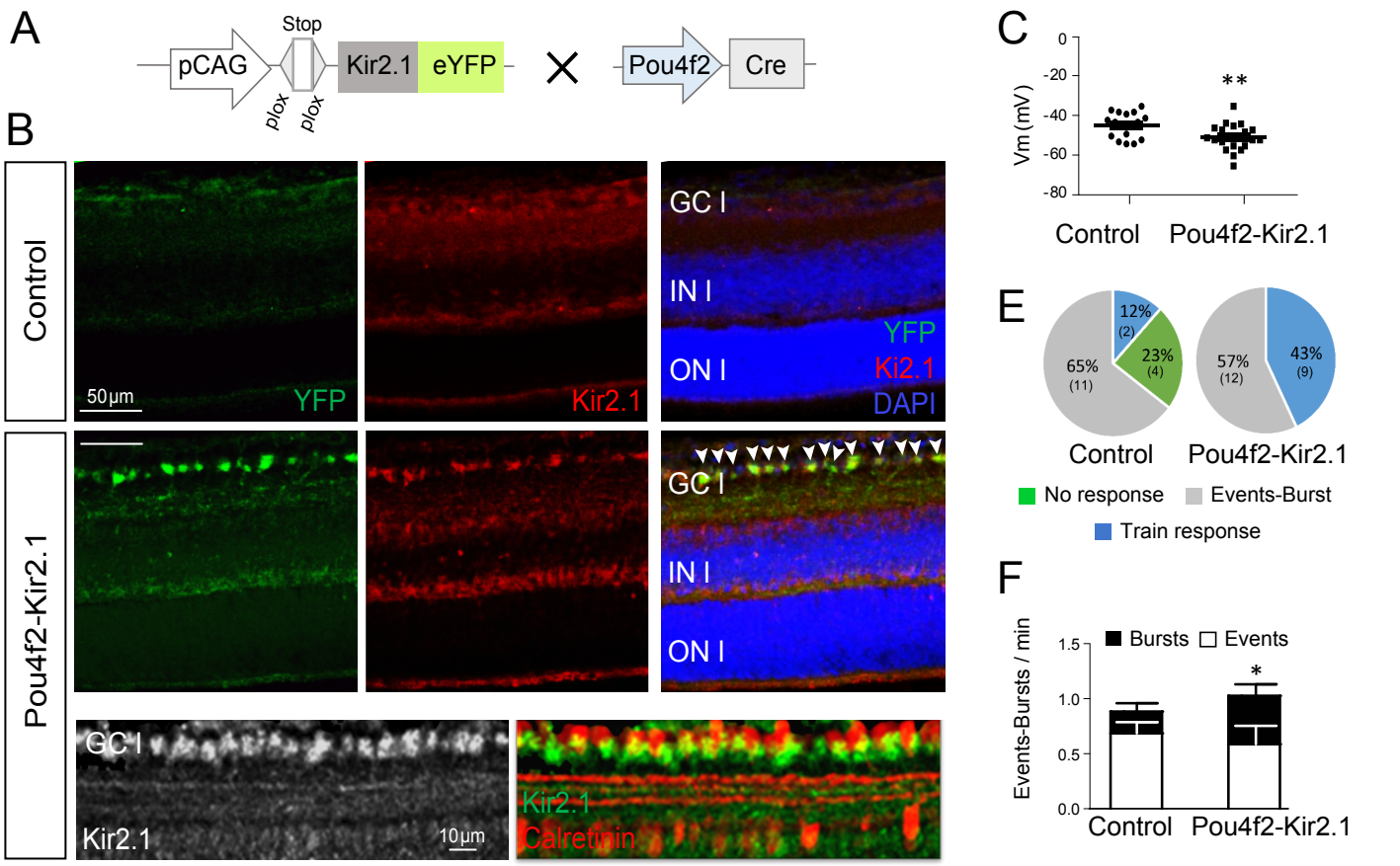
A
Stop
pCAG
plox
plox
Kir2.1
eYFP
Pou4f2
Cre
B
Control
Pou4f2-Kir2.1
50µm
YFP
Kir2.1
GC l
IN l
ON l
YFP
Ki2.1
DAPI
GC l
IN l
ON l
GC l
Kir2.1
10µm
Kir2.1
Calretinin
C
Vm (mV)
0
-20
-40
-60
-80
**
Control
Pou4f2-Kir2.1
E
12%
(2)
23%
(4)
65%
(11)
57%
(12)
43%
(9)
Control
Pou4f2-Kir2.1
No response
Events-Burst
Train response
F
Events-Bursts / min
Bursts
Events
1.5
1.0
0.5
0.0
*
Control
Pou4f2-Kir2.1

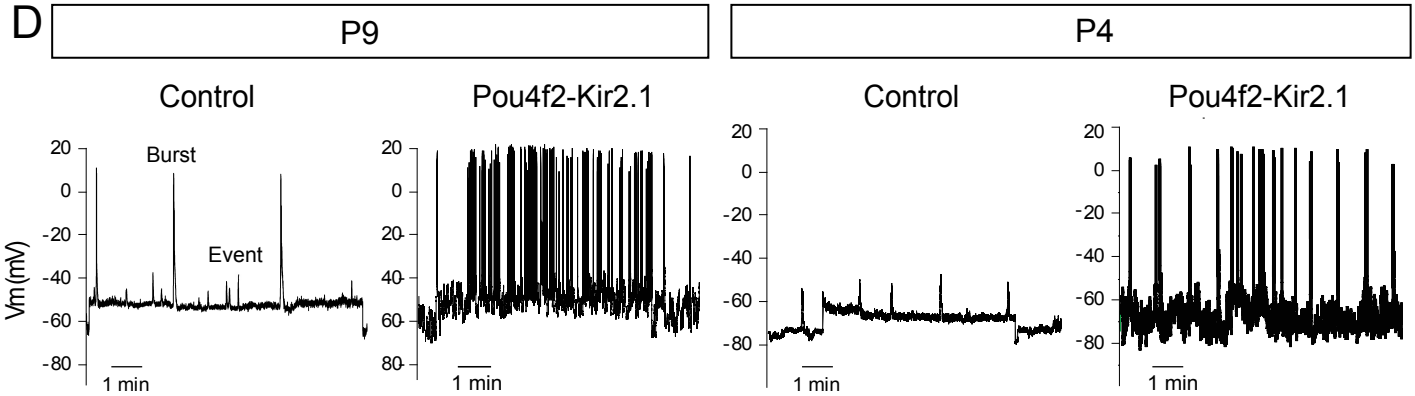
D
P9
P4
Control
Pou4f2-Kir2.1
Control
Pou4f2-Kir2.1
Vm (mV)
Burst
Event
20
0
-20
-40
-60
-80
1 min
20
0
20
40
60
80
1 min
20
0
-20
-40
-60
-80
1 min
20
0
-20
-40
-60
-80
1 min

Figure 1

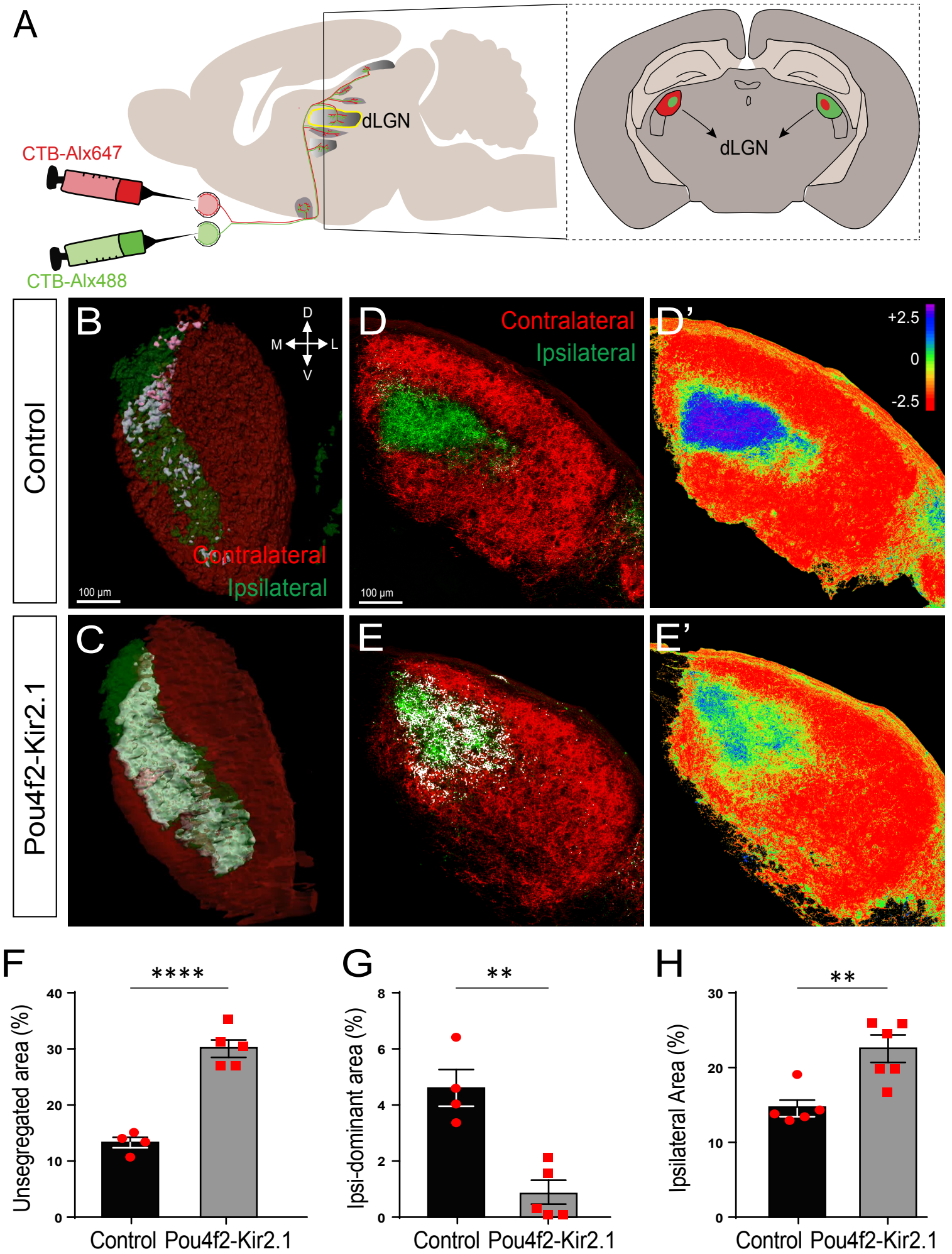
A
CTB-Alx647
CTB-Alx488
dLGN
dLGN
Control
Pou4f2-Kir2.1
B
D
M
L
V
Contralateral
Ipsilateral
100 µm
D
Contralateral
Ipsilateral
100 µm
D'
+2.5
0
-2.5
C
E
E'
F
****
Unsegregated area (%)
Control
Pou4f2-Kir2.1
G
**
Ipsi-dominant area (%)
Control
Pou4f2-Kir2.1
H
**
Ipsilateral Area (%)
Control
Pou4f2-Kir2.1

Figure 2

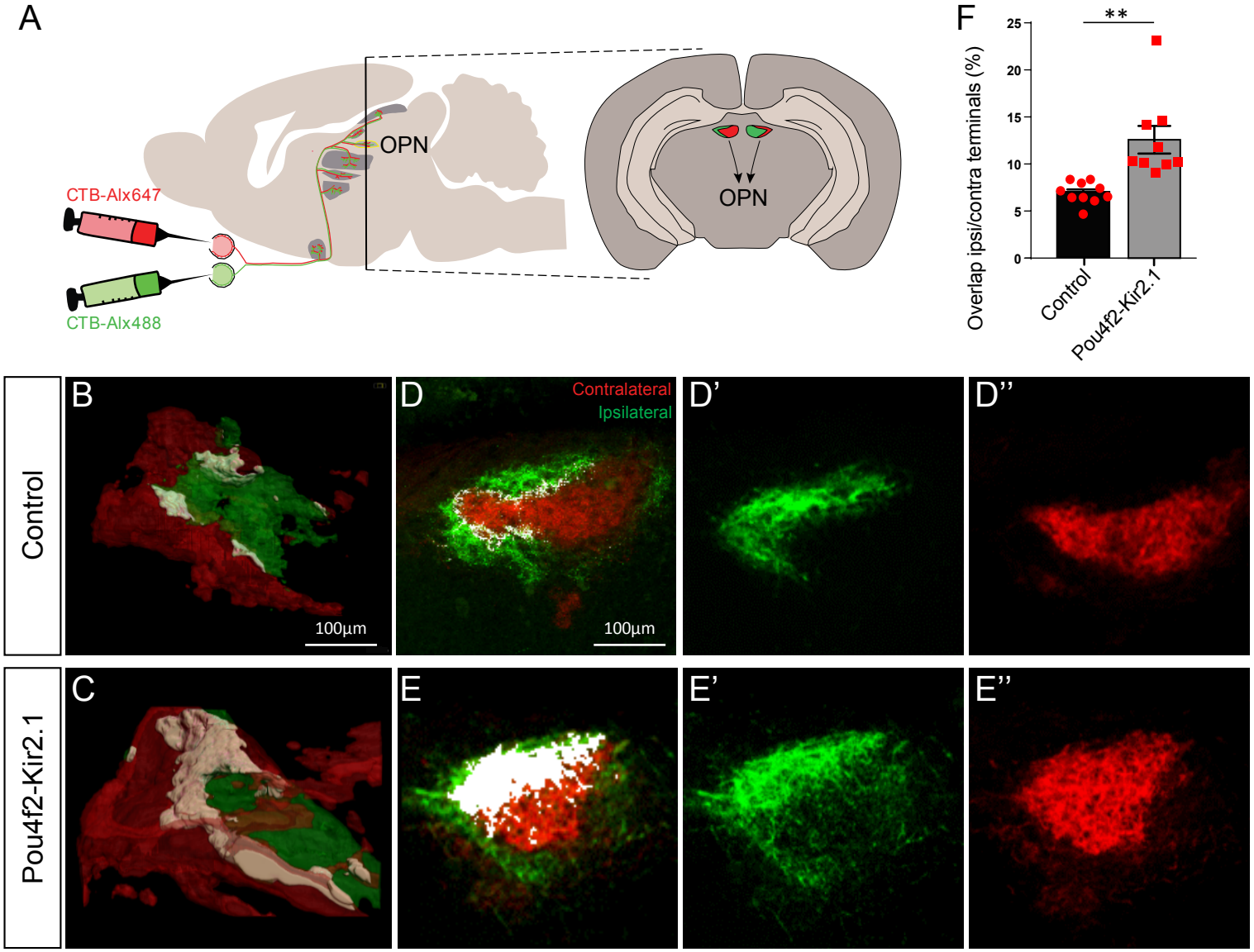
A
CTB-Alx647
CTB-Alx488
OPN
OPN
F
**
Overlap ipsi/contra terminals (%)
25
20
15
10
5
0
Control
Pou4f2-Kir2.1
Control
Pou4f2-Kir2.1
B
C
D
Contralateral
Ipsilateral
D'
D''
E
E'
E''
100µm
100µm

Figure 3

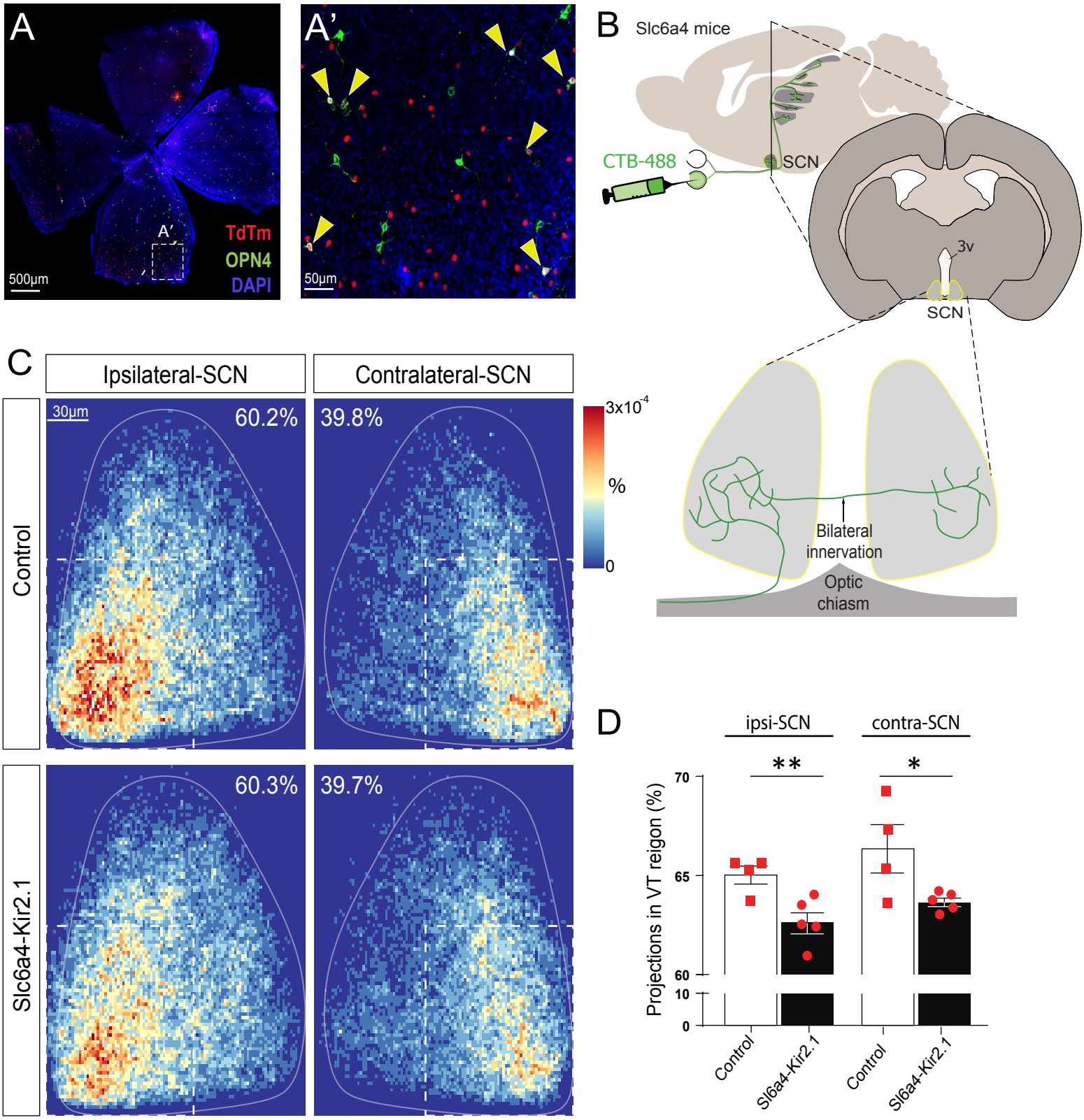
A
A'
TdTm
OPN4
DAPI
500µm
A'
50µm
B
Slc6a4 mice
CTB-488
SCN
3v
SCN
Bilateral
innervation
Optic
chiasm
C
Ipsilateral-SCN
Contralateral-SCN
Control
Slc6a4-Kir2.1
30µm
60.2%
39.8%
60.3%
39.7%
3x10-4
%
0
D
ipsi-SCN
contra-SCN
**
*
Projections in VT reigon (%)
70
65
60
10
0
Control
Sl6a4-Kir2.1
Control
Sl6a4-Kir2.1

Figure 4

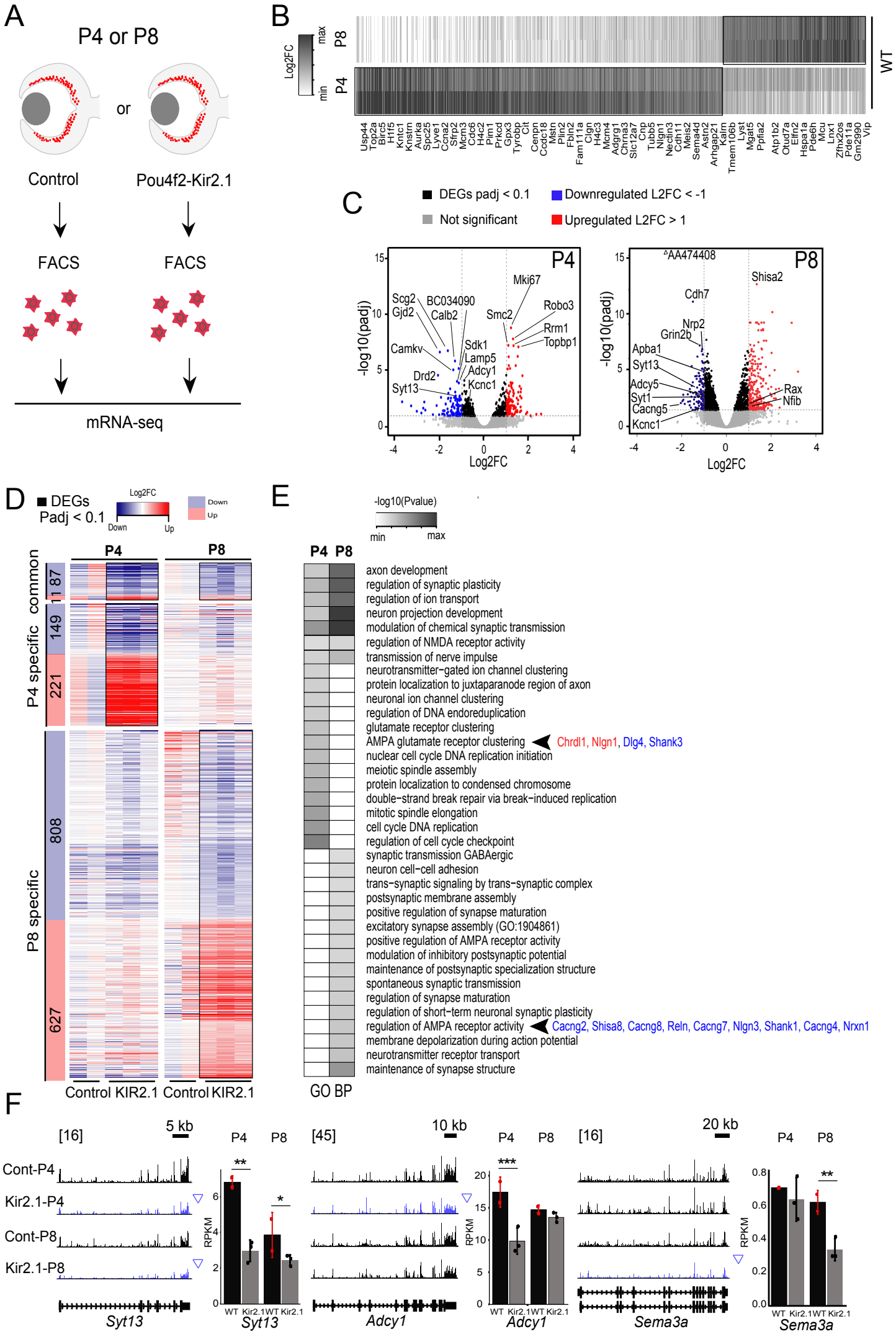
A
P4 or P8
or
Control
Pou4f2-Kir2.1
FACS
FACS
mRNA-seq
B
Log2FC
max
min
P8
P4
WT
Usp44 Top2a Birc5 Hif5 Kntc1 Knstrn Aurka Spc25 Lyve1 Ccna2 Sfrp2 Mcm3 Cdc6 H4c2 Pim1 Prkcd Gpx3 Tyrobp Clt Cenpn Ccdc18 Mstn Plin2 Fbln2 Fam111a Clgn H4c3 Mcm4 Adgrg1 Chrna3 Slc12a7 Cnp Tubb5 Nlgn1 Nectin3 Cdh11 Meis2 Sema4d Astn2 Arhgap21 Kalrn Tmem106b Lyst Mgat5 Ppfia2 Atp1b2 Otud7a Elfn2 Hspa1a Pde6h Mcu Lnx1 Zfhx2os Pde11a Gm2990 Vip
C
DEGs padj < 0.1
Downregulated L2FC < -1
Not significant
Upregulated L2FC > 1
P4
-log10(padj)
Log2FC
Scg2 Gjd2 BC034090 Calb2 Mki67 Smc2 Robo3 Rrm1 Topbp1 Sdk1 Lamp5 Adcy1 Kcnc1 Camkv Drd2 Syt13
P8
AA474408 Shisa2 Cdh7 Nrp2 Grin2b Apba1 Syt13 Adcy5 Syt1 Cacng5 Kcnc1 Rax Nfib
D
DEGs
Padj < 0.1
Log2FC
Down
Up
P4
P8
common
P4 specific
P8 specific
11 87
149
221
808
627
Control KIR2.1 Control KIR2.1
E
-log10(Pvalue)
min
max
P4 P8
GO BP
axon development
regulation of synaptic plasticity
regulation of ion transport
neuron projection development
modulation of chemical synaptic transmission
regulation of NMDA receptor activity
transmission of nerve impulse
neurotransmitter-gated ion channel clustering
protein localization to juxtaparanode region of axon
neuronal ion channel clustering
regulation of DNA endoreduplication
glutamate receptor clustering
AMPA glutamate receptor clustering
Chrdl1, Nlgn1, Dlg4, Shank3
nuclear cell cycle DNA replication initiation
meiotic spindle assembly
protein localization to condensed chromosome
double-strand break repair via break-induced replication
mitotic spindle elongation
cell cycle DNA replication
regulation of cell cycle checkpoint
synaptic transmission GABAergic
neuron cell-cell adhesion
trans-synaptic signaling by trans-synaptic complex
postsynaptic membrane assembly
positive regulation of synapse maturation
excitatory synapse assembly (GO:1904861)
positive regulation of AMPA receptor activity
modulation of inhibitory postsynaptic potential
maintenance of postsynaptic specialization structure
spontaneous synaptic transmission
regulation of synapse maturation
regulation of short-term neuronal synaptic plasticity
regulation of AMPA receptor activity
Cacng2, Shisa8, Cacng8, Reln, Cacng7, Nlgn3, Shank1, Cacng4, Nrxn1
membrane depolarization during action potential
neurotransmitter receptor transport
maintenance of synapse structure
F
[16]
5 kb
Cont-P4
Kir2.1-P4
Cont-P8
Kir2.1-P8
Syt13
P4 P8
RPKM
WT Kir2.1 WT Kir2.1
[45]
10 kb
Adcy1
[16]
20 kb
Sema3a

Figure 5

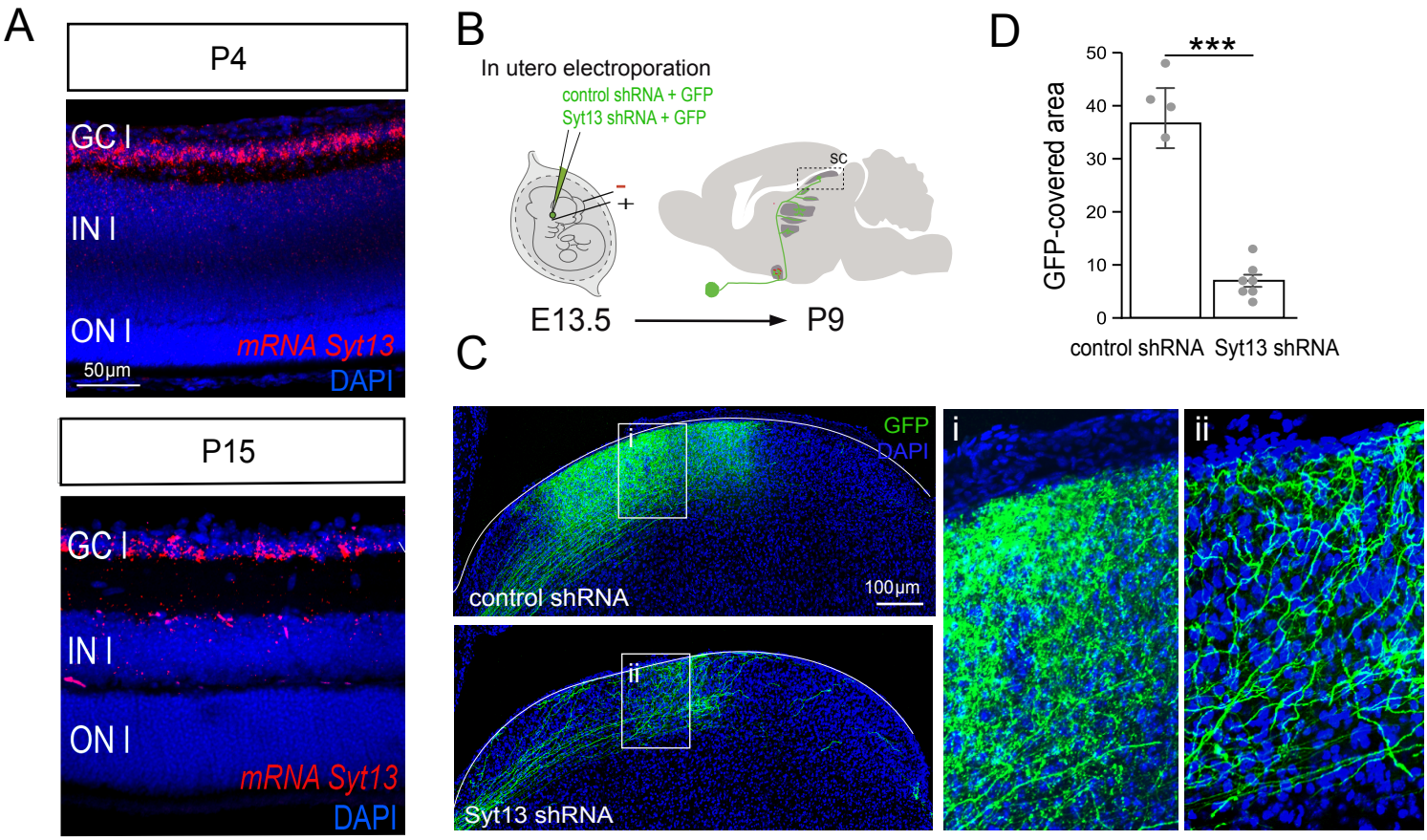
A
P4
GC l
IN l
ON l
mRNA Syt13
DAPI
50µm
P15
GC l
IN l
ON l
mRNA Syt13
DAPI
B
In utero electroporation
control shRNA + GFP
Syt13 shRNA + GFP
SC
E13.5
P9
C
GFP
DAPI
i
control shRNA
100µm
ii
Syt13 shRNA
i
ii
D
***
GFP-covered area
50
40
30
20
10
0
control shRNA
Syt13 shRNA

Figure 6